



EMPTY ROOM—©ISTOCKPHOTO.COM/TAMPATRA,
ROBOT PLATFORMS—©ISTOCKPHOTO.COM/TWILIGHTPRODUCTIONS

Robotic Through-Wall Imaging

Radio-frequency imaging possibilities with unmanned vehicles.

Saandeep Depatla,
Chitra R. Karanam, and
Yasamin Mostofi

Digital Object Identifier 10.1109/MAP.2017.2731302
Date of publication: 25 August 2017

Using electromagnetic waves for sensing has been of interest to the research community for many years. More recently, sensing with lower frequencies, such as with radio waves and even with Wi-Fi, has become of interest due to factors like safety and availability of the transceivers. In particular, there has been a considerable interest in using radio-frequency (RF) signals to sense and obtain information about the environment in various contexts, such as imaging, localization, tracking, and occupancy estimation [1]–[10]. See-through imaging (also known as *through-wall imaging*) has, in particular, been of considerable interest

to the research community. The ability to see through occluded objects can be beneficial to many applications, such as search and rescue, surveillance and security, archaeological discovery, detection/classification of occluded objects, and medical applications. Despite great interest in this area, however, see-through imaging is still a considerably challenging problem, especially with everyday RF signals.

UNMANNED VEHICLES FOR SEE-THROUGH IMAGING

Recent progress in robotics has created the possibility of unmanned autonomous vehicles helping us achieve tasks. Robotic networks can have a tremendous impact in many areas, such as disaster relief, emergency response, environmental monitoring, surveillance, and security.

In this article, we are interested in using unmanned vehicles for see-through imaging to enable imaging that is typically deemed not possible with static antennas. More specifically, we are interested in the scenario where two unmanned vehicles are tasked with imaging a completely unknown area, without any prior measurements, which we refer to as *robotic see-through imaging*. Figure 1(a) shows a real example of the considered scenario. We first focus on robotic through-wall imaging based on only Wi-Fi received signal strength indicator (RSSI) signals. In other words, in our first case, Wi-Fi received signal power is the only signal available for imaging. More specifically, both robots are equipped with Wi-Fi cards, and the receiving robot measures the received signal power of the transmitting robot. In our second case, we consider robotic imaging based on only ultrawideband (UWB) signals. While most UWB transceivers have been bulky and expensive, the new commercially available chipset from DecaWave [11] [see Figure 1(d)] provides a lightweight solution, with stable measurements for the power and time of arrival (ToA) of the first path, which we shall use in our second case.

See-through imaging is still a considerably challenging problem, especially with everyday RF signals.

LITERATURE SURVEY

A survey of the existing literature reveals a great body of work from various communities, e.g., electromagnetics, signal processing, and networking, on different aspects of RF sensing and through-wall imaging. In the electromagnetics community, for instance, there has been considerable interest in solving the

inverse scattering problem [12], [13]. More specifically, various full-wave solutions are obtained by using iterative techniques [14], contrast source inversion [15], and stochastic optimization [16]. Several linearizing approximations, such as Born and Rytov, are also proposed [2], [17], [18] to reduce the computational complexity in imaging. To reduce the number of required measurements, compressive sensing techniques have been used under these linear approximations [19]–[21]. However, there are very few experimental results reported with these approximations, especially at microwave frequencies or Wi-Fi, due to the difficulty of the hardware setup and testing.

Assuming that phase can be measured, beamforming and time-reversal multiple signal classification are proposed to focus in a direction or image a target [1], [22], [23]. Radar systems have also been extensively used for remote sensing and target detection [24], [25]. Synthetic aperture radar uses motion of the radar to synthesize a large antenna array to improve the resolution of remote sensing [26]. Using UWB signals can increase the resolution [3] but has traditionally required specialized and bulky hardware [27], making them unsuitable for small robotic platforms.

In general, several existing works use simulations for validation purposes due to the difficulty of the hardware setup and testing. Thus, the full benefits of the theoretical methods may not be realizable in real scenarios. Furthermore, for the case of through-wall imaging, the information of the first layer of occluders (such as the wall) is usually assumed via prior measurements [4], [28], [29]. Recently, a few methods propose to mitigate the effect of the walls [30]–[32].

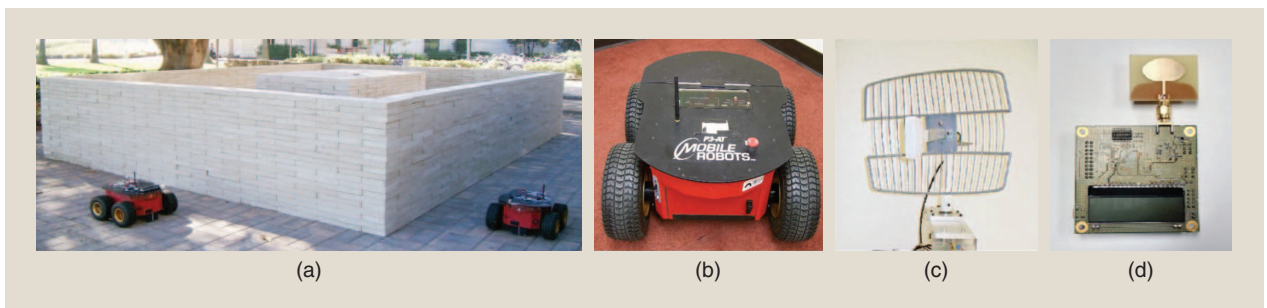


FIGURE 1. The experiment setup and the corresponding hardware components. (a) Two robots making measurements outside an unknown space to image the entire area, including both occluded and nonoccluded parts; (b) a Pioneer 3-AT robot, (c) a directional parabolic grid antenna (GD24-15 2.4 GHz) that will be used in some of the experiments when imaging with Wi-Fi; and (d) a DecaWave EVK1000 transceiver with an omnidirectional antenna, which will be used when imaging with UWB signals.

However, these methods typically have experimental constraints, either on the locations along which the measurements are collected or on the properties of the wall, and they are furthermore focused on localizing the objects as opposed to detailed imaging. Also, in most setups, sensors are on one side of the wall, and thus a reflection-based approach is typically used for through-wall imaging. Finally, several existing works rely on the availability of the phase information or having a very large bandwidth. Even then, the problem of see-through imaging of completely unknown areas with everyday RF signals is still a challenging problem, which is the main motivation for this article.

In this article, we show the possibilities and challenges created by using unmanned vehicles for through-wall imaging with ubiquitous RF signals. We do not assume any knowledge of the walls and, as such, reconstruct the walls as well. Using unmanned vehicles can considerably reduce the burden of fixed antenna positioning, as the vehicles can autonomously collect several RF measurements along their trajectories. More importantly, the fact that they have control over their trajectories has great potential for improving see-through imaging through proper path planning. Finally, because two unmanned vehicles move outside of the area of interest, they can do tomographic imaging, i.e., one robot transmits a signal, which will interact with the area of interest as it goes through it. The receiving robot then measures the corresponding receptions [see Figure 1(a) for an example]. Using the transmission through the area, as opposed to reflections, is more suitable when no phase measurement is assumed, which is the case in this article. In our past work, we showed the first demonstration of imaging with Wi-Fi in 2010 [33] and the first demonstration of through-wall imaging with Wi-Fi in 2012 [7], followed by several other works [8], [9]. In this article, we build on our past work to present a comprehensive foundation for imaging through walls with unmanned vehicles. Additionally,

- We propose a UWB-based robotic imaging approach based on the first-path power and ToA, and we experimentally and extensively validate it using new commercially available UWB chipsets from DecaWave. We further extensively compare Wi-Fi and UWB-based approaches.
- We show the impact of antenna directionality on the imaging quality. As we shall see, while using a directional antenna improves the imaging quality, through-wall imaging with omnidirectional antennas is also possible when using the proposed robotic framework.
- We analyze the impact of a large amount of robot localization error on the imaging performance. The results indicate robustness to localization errors, even for values with a standard deviation as high as 10 cm per position.
- We present several see-through experimental results involving objects with different material properties.

Overall, this article showcases the possibilities for imaging with everyday RF signals when using unmanned vehicles.

A FOUNDATION FOR ROBOTIC THROUGH-WALL IMAGING

PROBLEM FORMULATION

Consider a workspace \mathbf{D} that is completely unknown, i.e., it contains objects whose shapes, locations, or material property are completely unknown. Furthermore, several objects may be occluded by walls or other objects. Figure 2 shows an example of our considered scenario. Two robots come to outside of the area of interest. One of the robots transmits RF signals, while the other robot measures the corresponding received signal. These scattered signals interact with the unknown area and thus implicitly contain information about the objects in \mathbf{D} . Our objective is to use robots to image the unknown workspace \mathbf{D} , by which we mean determining the location and geometry of all the objects in \mathbf{D} , without any a priori measurements.

In this section, we start by summarizing the volume integral equations to model the received electric field in terms of the objects in \mathbf{D} and the positions of the transmitter (Tx) and receiver (Rx) robots. We then discuss linearizing approximations to formulate our problem as a linear inverse scattering problem, which we then solve to image \mathbf{D} using sparse signal processing and path planning. Consider the electric field in \mathbf{D} that is induced by the signal transmitted from the Tx robot. The following volume integral equation then characterizes the received electric field at any position $\mathbf{r} \in \mathbb{R}^3$ [34]:

$$\mathbf{E}(\mathbf{r}) = \mathbf{E}_{\text{inc}}(\mathbf{r}) + \iiint_{\mathbf{D}} \bar{\mathbf{G}}(\mathbf{r}, \mathbf{r}') \cdot (O(\mathbf{r}') \mathbf{E}(\mathbf{r}')) d\mathbf{v}', \quad (1)$$

where $\mathbf{E}(\mathbf{r})$ is the received electric field at \mathbf{r} , $\bar{\mathbf{G}}(\mathbf{r}, \mathbf{r}')$ is the free space tensor Greens function, $O(\mathbf{r}) = k^2(\mathbf{r}) - k_0^2$ denotes the material property of the object at position \mathbf{r} , $k_0^2 = \omega^2 \mu_0 \epsilon_0$ denotes the wavenumber of the free space, $k^2(\mathbf{r}) = \omega^2 \mu_0 \epsilon(\mathbf{r})$ denotes the wavenumber of the medium at \mathbf{r} , $\epsilon(\mathbf{r})$ denotes the

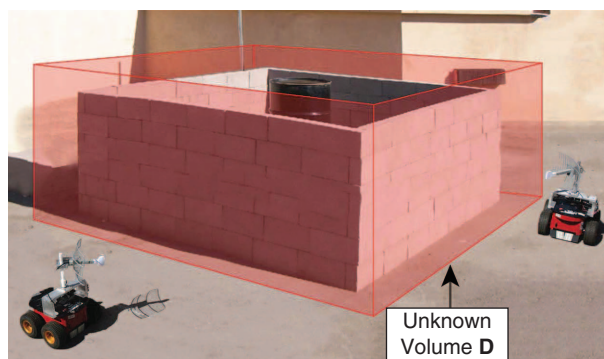


FIGURE 2. The objective of the robots is to image the completely unknown workspace \mathbf{D} , shown with a superimposed red volume. Note that there are several objects that are completely occluded by the outer brick walls, requiring through-wall imaging. In this article, we first consider robotic imaging based on only Wi-Fi RSSI signals, followed by robotic imaging based on only UWB signals.

electric permittivity at \mathbf{r} , ϵ_0 and μ_0 are the permittivity and permeability of the free space, respectively, ω is the angular frequency, \bullet denotes the vector dot product, and $\mathbf{E}_{\text{inc}}(\mathbf{r})$ is the incident field at \mathbf{r} when there are no objects in \mathbf{D} . The first term of (1) then describes the field due to the presence of a source, and the second term describes the field due to scattering from objects in \mathbf{D} . If the source is linearly polarized, then, by neglecting the cross-polarization terms in the scattered field, we can simplify (1) to the following scalar form [8]:

$$E(\mathbf{r}) = E_{\text{inc}}(\mathbf{r}) + \iiint_{\mathbf{D}} g(\mathbf{r}, \mathbf{r}') O(\mathbf{r}') E(\mathbf{r}') dv', \quad (2)$$

where $g(\mathbf{r}, \mathbf{r}')$ is the scalar Greens function.

LINEARIZING APPROXIMATIONS

Equation (2) relates the received electric field $E(\mathbf{r})$ to the objects in \mathbf{D} . However, because the field $E(\mathbf{r}')$ inside the integral of (2) depends on $O(\mathbf{r}')$, (2) can be highly nonlinear in \mathbf{D} due to multiple scattering [34]. As discussed in the ‘‘Unmanned Vehicles for See-Through Imaging’’ section, full-wave solutions can be obtained for (2) [14]–[16]. However, these methods have prohibitive computational complexity, especially for the sizes of the workspace \mathbf{D} considered in this article. Therefore, we use approximations to linearize and then solve (2) by using proper robotic path planning and sparse signal processing. These approximations only consider single scattering from objects in \mathbf{D} , neglecting multiple scattering [34]. Next we present two such approximations, which will work well for our robotic see-through imaging.

LINE-OF-SIGHT APPROXIMATION

At high frequencies (in this article, *high frequency* refers to the frequencies at which the size of the inhomogeneity of the objects is much larger than the wavelength), a wave predominantly propagates in a straight line, with negligible reflections or diffractions along its path [34]. Then a line-of-sight (LOS)-based approximation (also referred to as *WKB approximation* [34]) can model the field well, and we can assume that the field at the Rx only depends on objects along the line joining the Tx and the Rx, which results in the following solution to (2) [34]:

$$E(\mathbf{r}) = \frac{c_0}{\sqrt{\alpha(\mathbf{r})}} e^{j\omega \int_{L_{T-R}} \alpha(\mathbf{r}') d\mathbf{r}'}, \quad (3)$$

where $\alpha(\mathbf{r})$ is a complex number that represents the slowness of the medium at \mathbf{r} and is related to $k(\mathbf{r})$, $\int_{L_{T-R}}$ is a line integral along the line joining the positions of the Tx and the Rx, and c_0 is a constant that depends on the transmitted signal strength. In this article, however, we assume Wi-Fi frequencies such as 2.4 GHz, which is not high enough. Still, the LOS-based approximation can be informative for our robotic imaging problem, as we shall see in the next sections. The received power is then given by the following [8]:

$$P_r(\mathbf{r})(\text{dBm}) = P_{\text{inc}}(\mathbf{r})(\text{dBm}) - 10 \log_{10}(e^2) \omega \int_{L_{T-R}} \text{Imag}(\alpha(\mathbf{r}')) d\mathbf{r}', \quad (4)$$

where $P_r(\mathbf{r})(\text{dBm})$ is the received power in dBm at \mathbf{r} , $P_{\text{inc}}(\mathbf{r})(\text{dBm})$ is the power incident in dBm at \mathbf{r} when there are no objects in \mathbf{D} , and $\text{Imag}(\cdot)$ denotes the imaginary part of the argument. $P_{\text{inc}}(\mathbf{r})(\text{dBm})$ can be estimated by robots making measurements in free space [8]. By discretizing the space and, subsequently, (4), we get the following linear equation:

$$\mathbf{P} \approx A_{\text{LOS}} \mathbf{O}_L, \quad (5)$$

where $\mathbf{P} = ((P_r(\text{dBm}) - P_{\text{inc}}(\text{dBm}))/10 \log_{10}(e^{-2}))$, A_{LOS} is a matrix of size $M \times N$ with its entry $A_{\text{LOS},ij} = 1$ if the j th cell is along the line joining the Tx and Rx of the i th measurement, and $A_{\text{LOS},ij} = 0$ otherwise, M and N denote the number of measurements and size of the discretized unknown space, respectively, $\mathbf{O}_L = [\alpha_1(\mathbf{r}_1) \alpha_1(\mathbf{r}_2) \cdots \alpha_1(\mathbf{r}_N)]^T$, $\mathbf{r}_1, \mathbf{r}_2 \cdots \mathbf{r}_N$ denote the positions of the cells in the workspace, and $\alpha_1(\cdot) = \text{Imag}(\alpha(\cdot))$.

RYTOV APPROXIMATION

Although the LOS-based approximation accounts for single scattering from objects in \mathbf{D} , only those objects along the LOS are considered. To incorporate the effect of scattering from all the objects in \mathbf{D} in a linear model, we next consider the Rytov approximation [34]. Then, the solution to (2) is approximated by

$$E(\mathbf{r}) = E_{\text{inc}}(\mathbf{r}) e^{j\phi(\mathbf{r})}, \quad (6)$$

where

$$\phi(\mathbf{r}) = \frac{-j}{E_{\text{inc}}(\mathbf{r})} \iiint_{\mathbf{D}} g(\mathbf{r}, \mathbf{r}') O(\mathbf{r}') E_{\text{inc}}(\mathbf{r}') dv'. \quad (7)$$

We then have the following approximation for the received power for this case [8]:

$$\mathbf{P} \approx A_{\text{Ryt}} \mathbf{O}_R, \quad (8)$$

where $\mathbf{O}_R = \text{Real}(\mathbf{O})$ and $\text{Real}(\cdot)$ denotes the real part of the argument. Detailed analysis of the validity of these approximations can be found in [34].

ROBOTIC THROUGH-WALL IMAGING

In this section, we first focus on robotic through-wall imaging based on only Wi-Fi RSSI signals in the ‘‘Robotic Through-Wall Imaging Using Only Wi-Fi RSSI Signals’’ section, providing an overview of the formulation of [8]. In other words, in our first case, Wi-Fi RSSI signals are the only signals available for imaging. More specifically, both robots are equipped with Wi-Fi cards, and the Rx robot measures the received signal power from the transmissions of the Tx robot. This case is important, as Wi-Fi cards are readily available and the RSSI signal can be easily measured in the Rx.

In our second case, in the ‘‘Robotic Through-Wall Imaging Using Only UWB Signals’’ section, we consider robotic imaging based on UWB signals. This case is motivated by the emergence of small UWB chipsets that can be easily added

to a small robotic platform, as discussed in the “Unmanned Vehicles for See-Through Imaging” section. We then extensively compare these two cases in the next section. We next briefly discuss these cases in the context of the previous linear approximations.

ROBOTIC THROUGH-WALL IMAGING USING ONLY WI-FI RSSI SIGNALS

In this case, (5) or (8) can be directly used. More formally, we will have [7], [8]

$$\mathbf{P}_{\text{Wi-Fi}} = \mathbf{A}\mathbf{X}, \quad (9)$$

where $\mathbf{P}_{\text{Wi-Fi}}$ is the accumulated vector of the received RSSI measurements as the robots move outside the area. Matrix \mathbf{A} is \mathbf{A}_{LOS} for the LOS case and \mathbf{A}_{Ryt} for the Rytov case. Then, we solve for \mathbf{X} , which will be the estimated image. Although the estimated \mathbf{X} will be an estimate of \mathbf{O}_{L} for the LOS case and \mathbf{O}_{R} for the Rytov case, both are nonzero at locations where there are objects and zero otherwise, allowing us to image the area.

ROBOTIC THROUGH-WALL IMAGING USING ONLY UWB SIGNALS

For the case of UWB transceivers, we use power of the first arrived path as well as its corresponding ToA. These two measurements are reliably provided by the new small UWB cards. It should be noted that, in a general UWB transceiver, one can measure the power-delay profile (ToA and power of a number of paths). However, we find the power-delay profile measurement not as stable in the small UWB chipset [11], Decawave EVK1000, as also reported by other users [35]. Thus, in this article, we only rely on using the power and ToA of the first path, which can be reliably measured in Decawave EVK1000 cards.

The scattered power of the first path is typically affected by the objects near and along the line joining the transceivers. Thus, the LOS-based modeling of the “Robotic Through-Wall Imaging” section can well approximate this case, as follows:

$$\mathbf{P}_{\text{UWB,FP}} \approx \mathbf{A}_{\text{LOS}}\mathbf{X}_{\text{P}}, \quad (10)$$

where $\mathbf{P}_{\text{UWB,FP}}$ is the received power of the first path of the UWB signal, \mathbf{A}_{LOS} is as defined in the “Problem Formulation” section, and you solve for the image vector \mathbf{X}_{P} .

Next, we consider the ToA of the first path that reaches the Rx in each transmission. The time taken for a signal to travel a distance δ through a homogeneous material of permittivity ϵ is given by $\delta\sqrt{\epsilon}/c$ [36], where c is the speed of light, and $\epsilon' = \text{Real}(\epsilon/\epsilon_0)$. Let $t_1(\mathbf{p}_i, \mathbf{q}_i)$ and $t_0(\mathbf{p}_i, \mathbf{q}_i)$ denote the ToA of the first path and the ToA in free space, respectively, where \mathbf{p}_i and \mathbf{q}_i denote the locations of the Tx and Rx, respectively for the i th measurement. Then, the difference between these times will be as follows:

$$t(\mathbf{p}_i, \mathbf{q}_i) = t_1(\mathbf{p}_i, \mathbf{q}_i) - t_0(\mathbf{p}_i, \mathbf{q}_i) = \int_{L_{T-R}} \frac{\sqrt{\epsilon'(\mathbf{r})} - 1}{c} d\mathbf{r}. \quad (11)$$

By discretizing (11), we get

$$t(\mathbf{p}_i, \mathbf{q}_i) = \sum_{j \in L_i} \frac{\Delta d}{c} (\sqrt{\epsilon'_j} - 1), \quad (12)$$

where L_i is the set of all the cells that lie on the line joining the Tx and Rx for the i th measurement, $i \in \{1, 2, \dots, M\}$, M is the number of measurements, Δd is the cell size, $\epsilon'_j = \epsilon'(\mathbf{r}_j)$, and \mathbf{r}_j is the position of the j th cell. The discretization is made small enough so that each cell can be assumed homogeneous, having the same permittivity throughout the cell. By stacking up all the measurements, we get the following linear equation for the ToA of the first path:

$$\mathbf{T}_{\text{UWB}} \approx \mathbf{A}_{\text{LOS}}\mathbf{\Lambda}, \quad (13)$$

where $\mathbf{\Lambda}$ represents the relative times to be estimated, with the key feature that its corresponding value will be zero if there is no object at the corresponding position and nonzero otherwise, allowing us to form an image of the area from the estimate of $\mathbf{\Lambda}$.

Let $\hat{\mathbf{X}}_{\text{UWB,p}}$ and $\hat{\mathbf{\Lambda}}_{\text{UWB,t}}$ be the solutions of (10) and (13), respectively. Although $\hat{\mathbf{X}}_{\text{UWB,p}}$ and $\hat{\mathbf{\Lambda}}_{\text{UWB,t}}$ represent different physical properties of the objects in \mathbf{D} , both solutions are nonzero at locations where there is an object and zero otherwise. Thus, we can jointly use them to image the objects as follows:

$$\hat{\mathbf{X}}_{\text{UWB}} = f(\hat{\mathbf{X}}_{\text{UWB,p}}, \hat{\mathbf{\Lambda}}_{\text{UWB,t}}), \quad (14)$$

where f is a function that efficiently combines the information in $\hat{\mathbf{X}}_{\text{UWB,p}}$ and $\hat{\mathbf{\Lambda}}_{\text{UWB,t}}$, and $\hat{\mathbf{X}}_{\text{UWB}}$ is the overall estimate of the unknown space. More details on f are given in the “Experimental Results” section.

SPARSE SIGNAL PROCESSING AND IMAGE RECONSTRUCTION

In the previous section, we posed a number of linear equations that related the measurements to the properties of the objects in the unknown space. Let N and M denote the size of the discretized space and the total number of measurements, respectively. Typically, due to the size of workspace of interest to this article and the difficulty of collecting a prohibitive number of measurements, we will have $M \ll N$. This leads to an underdetermined system of equations in (9), (10), and (13). Therefore, to get a meaningful solution to these equations, we need to take advantage of the underlying sparsity of the area of interest. More specifically, many real physical spaces are sparse in the space domain or in their spatial variations [7], allowing us to use tools from sparse signal processing [37], which we briefly summarize next. Consider the following general linear equation:

$$\mathbf{Y} = \mathbf{B}\mathbf{Z}, \quad (15)$$

where $\mathbf{Z} \in \mathbb{R}^N$ is a general unknown signal, $\mathbf{Y} \in \mathbb{R}^M$ is the measurement vector, and \mathbf{B} is an $M \times N$ observation matrix. Suppose \mathbf{Z} is sparse in some domain, i.e.,

$$\mathbf{Z} = \Theta \mathbf{z}, \quad (16)$$

where Θ is an invertible matrix and \mathbf{z} is S sparse, i.e., $\text{card}(\text{supp}(\mathbf{z})) = S$, where $\text{card}(\cdot)$ denotes the cardinality of the argument and $\text{supp}(\cdot)$ denotes the set of indices of the nonzero elements of the argument. If $N \geq 2S$, then the solution to (15), under specific conditions [37], is given by the following optimization problem:

$$\text{minimize } \|\mathbf{z}\|_0, \quad \text{subject to } \mathbf{Y} = \mathbf{Kz}, \quad (17)$$

where $\mathbf{K} = \mathbf{B}\Theta$. This means we only require $2S$ measurements to recover \mathbf{Z} . However, the preceding problem is nonconvex and combinatorial in nature. The following is the convex relaxation of the problem:

$$\text{minimize } \|\mathbf{z}\|_1, \quad \text{subject to } \mathbf{Y} = \mathbf{Kz}. \quad (18)$$

In the compressive sensing literature [37]–[39], it has been well established that solving (18) can solve the original problem of (17) if the matrix \mathbf{K} satisfies the restricted isometry condition (RIC) [39]. In the context of our considered robotic through-wall imaging, we have shown that certain motion patterns result in a matrix \mathbf{K} that satisfies the RIC condition in [7]. Several of the considered areas are also sparse in their spatial variations. Thus, minimizing the spatial variation can also provide an alternative to the ℓ_1 relaxation, with a lower computational complexity [7]. In this article, we thus focus on total variation (TV) minimization. More specifically, let $R = [R_{i,j}]$ denote an $m \times n$ matrix that represents the unknown space. Then we solve the following TV minimization problem:

$$\text{minimize } \text{TV}(R), \quad \text{subject to } \mathbf{Y} = \mathbf{Kz}, \quad (19)$$

where $\text{TV}(R) = \sum_{i,j} \|D_{i,j}(R)\|$, denotes the spatial variations of the unknown space, where

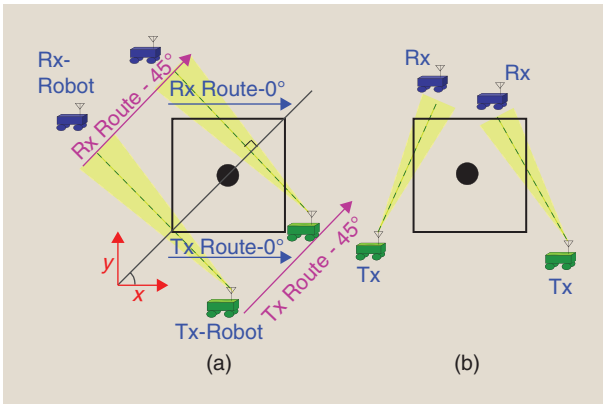


FIGURE 3. An illustration of (a) semiparallel robotic routes, and (b) random routes, as defined in [8]. (a) Shows sample semiparallel routes at 0 and 45°. Random routes refer to routes that do not have a specific pattern.

$$D_{i,j}(R) = [D_{h,i,j} \ D_{v,i,j}],$$

$$D_{h,i,j} = \begin{cases} R_{i+1,j} - R_{i,j} & \text{if } 1 \leq i < m, \\ R_{i,j} - R_{1,j} & \text{if } i = m, \end{cases},$$

$$D_{v,i,j} = \begin{cases} R_{i,j+1} - R_{i,j} & \text{if } 1 \leq j < n, \\ R_{i,j} - R_{i,1} & \text{if } j = n \end{cases},$$

and $D_{h,i,j}$ and $D_{v,i,j}$ denote the spatial variations in the horizontal and vertical directions, respectively. The linear equation of (19) can then represent (9), (10), or (13). We make use of MATLAB-based solver TVL3 [40] to solve the preceding optimization problem in the next sections.

The solution obtained by solving this optimization problem corresponds to a grayscale image reconstruction of the unknown space. Because we are only interested in imaging the locations and shapes of the objects (as opposed to the material properties), we further make use of the two-level Otsu thresholding method [41] in the next section. By using the Otsu method, the cells in the unknown space are optimally classified as empty or occupied, thereby providing a binary object image of the unknown area.

ROBOTIC PATH PLANNING

The main strengths of using unmanned vehicles for through-wall imaging are twofold: 1) the Tx and Rx antennas can be easily and autonomously positioned in many locations along a trajectory of the robots, a task that is prohibitive and challenging without unmanned vehicles, and 2) through proper path planning, the Tx and Rx locations can be properly optimized to be those most informative for imaging. More specifically, the paths that the robots take directly affect matrix \mathbf{K} in (19) and thus the imaging quality considerably. We next summarize two possible motion patterns of [8], [9]. In the first pattern, which is motivated by computed tomography, the robots take routes that we refer to as *semiparallel*. More specifically, consider the workspace of Figure 3(a) and the line that passes through the origin at angle θ . We say that the robots are taking a semiparallel route at angle θ if the Tx and Rx robots move such that the line connecting the two is orthogonal to the line that passes through the origin at the angle θ . Figure 3(a) shows two such sample routes at 0° and 45°. Note that the robots do not have to necessarily move in parallel. Thus, we refer to this pattern as semiparallel.

Then, the nonzero elements in each row of matrix \mathbf{K} correspond to the pixels in the unknown space that are visited by the line joining the Tx and Rx. As we shall see in the “Robotic Path Planning for Imaging” section, semiparallel routes can be very informative for robotic imaging. Thus, in the next section, we first show several experimental results with such routes. We then extensively summarize the interplay between path planning and robotic imaging in the “Robotic Path Planning for Imaging” section. In addition to semiparallel routes, we also consider the case where the Tx and Rx robots do not take a specific pattern and take wireless measurements

anywhere possible. This case is referred to as a *random motion pattern*. We emphasize that the robots do not necessarily have to take a randomized route, but random here means that no specific pattern is taken. Figure 3(b) shows an example of the random case. We then use the random pattern in the “Robotic Path Planning for Imaging” section, in conjunction with semiparallel routes, to discuss the underlying tradeoffs in path planning and robotic imaging.

EXPERIMENTAL RESULTS

In the “A Foundation for Robotic Through-Wall Imaging” section, we extensively discussed through-wall imaging based on either only Wi-Fi RSSI signals or only UWB signals (first-path power and ToA). In this section, we show the performance of this framework with several real structures. We start by summarizing our experimental setup.

SUMMARY OF EXPERIMENTAL SETUP

Our setup consists of two Pioneer 3-AT mobile robots [42], shown in Figure 1(b), which move outside of the unknown area of interest and collect wireless measurements. Figure 1(a) shows one example where the robots are making measurements in a real environment to image a completely unknown area. The robots are programmed to autonomously move along any set of given routes and collect wireless measurements.

When moving outside of the area of interest, the two robots do not coordinate their movement. Rather, each one traverses its given trajectory and estimates its own position and the position of the other robot based on the assumed constant speed. Our current localization error is less than 2.5 cm for every 1 m of straight-line movement. For the lengths of routes considered in this article, [8] shows that localization errors and the associated antenna alignment errors (when directional antennas are used) have a negligible impact on the reconstruction quality of the image.

IMAGING WITH ONLY WI-FI RSSI SIGNALS

In this case, we use the experimental setup described in [8]. We briefly summarize the setup here. The Tx robot is equipped with a WBR-1310 wireless router, which acts as a Wi-Fi signal source. The Rx robot is equipped with an on-board IEEE 802.11g wireless network card (Atheros ar5006x) that can measure Wi-Fi RSSI signals. As the robots move, the Tx robot continuously transmits Wi-Fi signals at +15 dBm. The signals are then measured by the Wi-Fi card on the Rx robot.

In some of the experiments with Wi-Fi, we use directional antennas to limit scattering from objects that are not on the direct LOS. In this case, we use a GD24-15 2.4-GHz parabolic grid antenna from Laird Technologies [43] for wireless

The robots are programmed to autonomously move along any set of given routes and collect wireless measurements.

transmissions, which is shown in Figure 1(c). This model has a 15-dBi gain with 21° horizontal and 17° vertical beamwidth.

IMAGING WITH ONLY UWB SIGNALS

For through-wall imaging with UWB signals, we mount a DecaWave EVK1000 transceiver chip [11] that is equipped with omnidirectional antennas on each robot. The transceiver, shown in Figure 1(d), supports

transmissions in six of the UWB channels outlined in the IEEE 802.15.4-2011 standard [44]. We use UWB transmissions at 3.99-GHz center frequency with a bandwidth of 900 MHz. This setup provides us with the power and ToA of the first path reaching the Rx, which we shall use for imaging.

Next, we present the performance of the through-wall imaging approach using this setup. We present Wi-Fi-based imaging results for two new areas, along with two Wi-Fi results considered in our previous work (albeit with some improvement using Otsu’s method) [7]–[9]. In the “Experimental Imaging Results with UWB Signals” section, we then show imaging results with only UWB signals. We further compare the performance of imaging based on Wi-Fi RSSI and imaging based on UWB signals. In the “Imaging of More Complex Areas” section, we present imaging of more complicated areas. Finally, in the “Impact of Antenna Directionality” section, we show the impact of antenna directionality on imaging based on Wi-Fi RSSI signals by comparing the results of imaging with omnidirectional and directional antennas. We note that, in all the results of this article, we only consider imaging of an unknown area in two dimensions, i.e., we only image a horizontal cut of the unknown area. We, however, emphasize that the methodology of this article can be generalized to three-dimensional imaging as well [10].

EXPERIMENTAL IMAGING RESULTS WITH WI-FI RSSI SIGNALS

Figure 4(a) shows the area of interest that is completely unknown, while Figure 4(b) shows a horizontal cut of it. The unknown area to be imaged is marked with a red dashed-line boundary in two dimensions. We refer to this area as the *occluded cylinder*. The cylinder is metallic, and the outer wall is made of concrete blocks. Note that the outer wall is also unknown and needs to be imaged. The size of the unknown area is 5.4 m × 5.4 m, with each pixel being 2 cm × 2 cm. Thus, the total number of unknowns amounts to 72,900. Two robots move outside of this area taking four semiparallel routes that are explained in the “Robotic Path Planning” section, along 0, 90, 45, and 135°. We use LOS-based approximation of (5) in this section. Furthermore, the robots use the directional antennas of Figure 1(c) for all Wi-Fi-based results of this section. We show results with Wi-Fi RSSI and omnidirectional antennas in the “Impact of Antenna Directionality” section.

Figure 4(c) shows the reconstruction with only 1.41% Wi-Fi RSSI measurements (a cruder result for imaging this

area with Wi-Fi was shown in [8]). The percentage measurement refers to the ratio of the total number of wireless measurements to the total number of unknowns (number of pixels of the unknown discretized space, e.g., 72,900 for Figure 4) when expressed as a percentage. Two-level Otsu's thresholding method is used to obtain a binary reconstruction of the unknown area. Even with such a very small percentage of measurements, the locations and shapes of the objects are imaged well. For instance, the center of the cylinder is imaged at the distance of 2.65 m from the top [see Figure 4(c)], which is very close to the true distance of 2.69 m.

We next consider imaging another completely unknown area, where the cylinder in Figure 4 is replaced by a human. Figure 5(a) shows the new considered scenario, with the human inside, while Figure 5(b) shows a horizontal cut of it. We refer to this area as the *occluded human*. We use robotic routes identical to that of the occluded cylinder to collect wireless measurements, which results in 1.41% measurements. Figure 5(c) shows the reconstructed image, which is thresholded as described previously. Similarly, we see that the objects are imaged with a good accuracy [compare the 2.66-m imaged distance in Figure 5(c) with the 2.69-m true distance of Figure 5(b)]. It is noteworthy that the reduction in the size of the occluded object (when going from the cylinder to the human) is well reflected in the reconstructed images. Overall, the robotic framework can image (image-through) highly

attenuating objects like concrete walls, metallic objects, and humans with high quality.

EXPERIMENTAL IMAGING RESULTS WITH UWB SIGNALS

Next, we show the imaging results for the occluded cylinder and occluded human with UWB signals. As shown in (14), our UWB imaging is based on both the ToA ($\hat{\Lambda}_{\text{UWB,t}}$) and power of the first path ($\hat{\mathbf{X}}_{\text{UWB,p}}$). These images are thresholded using the two-level Otsu's thresholding method. As for combining the two resulting images, i.e., choice of f in (14), we use the following approach. We consider a location in the final estimated image empty if the corresponding location in the thresholded $\hat{\Lambda}_{\text{UWB,t}}$ or $\hat{\mathbf{X}}_{\text{UWB,p}}$ is empty. Otherwise, we average the corresponding estimated intensity values to indicate the intensity of the object at that location followed by Otsu thresholding.

Figures 4(d) and 5(d) show the reconstructed images for the cases of the occluded cylinder and occluded human, respectively. The routes and the number of transmissions are the same as for the case of Wi-Fi RSSI of the "Experimental Imaging Results with Wi-Fi RSSI Signals" section. As shown, the imaging quality is considerably high for both scenarios. As compared to the Wi-Fi RSSI imaging results of the "Experimental Imaging Results with Wi-Fi RSSI Signals" section, the imaging results are comparable. This is because we used directional antennas for the Wi-Fi case of the the "Experimental Imaging Results with Wi-Fi RSSI Signals" section,

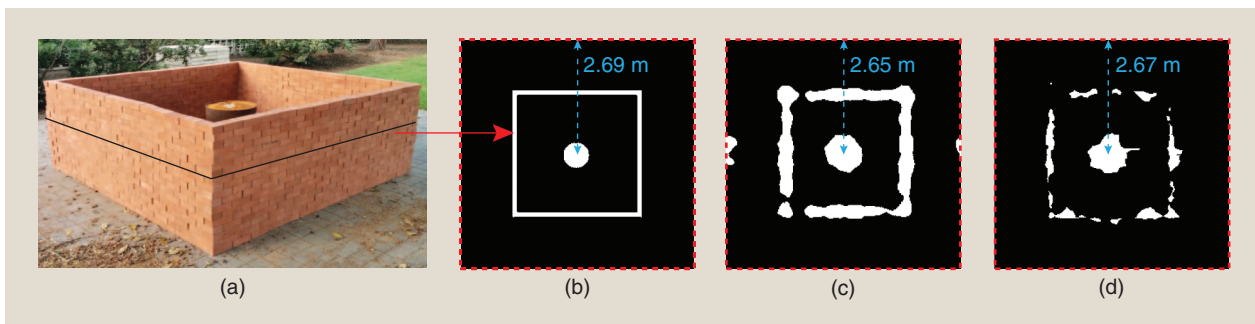


FIGURE 4. (a) The area of interest that is completely unknown, (b) a two-dimensional (2-D) horizontal cut of it, which has the dimensions $5.4 \text{ m} \times 5.4 \text{ m}$, with the red dashed lines indicating the boundary of the unknown area to be imaged, (c) reconstructed image with 1.41% Wi-Fi RSSI measurements using LOS-based approximation, and (d) reconstructed image with 1.41% UWB transmissions.

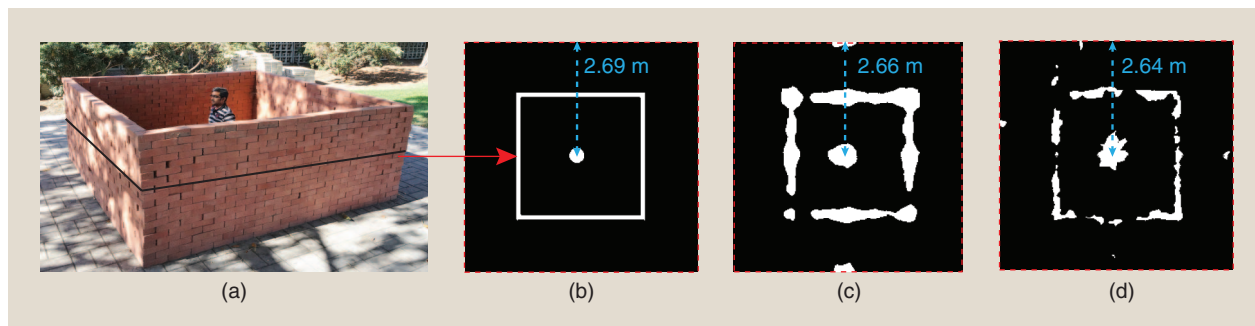


FIGURE 5. (a) The area of interest that is completely unknown, (b) a 2-D horizontal cut of it, which has the dimensions $5.4 \text{ m} \times 5.4 \text{ m}$, with the red dashed lines indicating the boundary of the unknown area to be imaged, (c) reconstructed image with 1.41% Wi-Fi RSSI measurements using LOS-based approximation, and (d) reconstructed image with 1.41% UWB transmissions.

which limits the scattering from objects out of the LOS path, making the results comparable to the case of imaging with the first path/ToA of UWB signals. However, as the antennas get more directional, their size increases, and it becomes difficult to use them with small mobile platforms. Thus, the UWB card of Figure 1(d), which is used in the experiments of this section, can be a promising choice for very small robotic platforms due to its small size (7 cm × 11 cm). Note that we do not even use the full capabilities of UWB signals here, such as multiple frequencies and delay spread, as explained in the earlier sections. We note that, while the total number of transmissions is the same for the Wi-Fi results of the “Experimental Imaging Results with Wi-Fi RSSI Signals” section and the UWB results of this section, the case of UWB also uses the ToA information, which doubles the number of linear equations to be used [(10) and (13)].

IMAGING OF MORE COMPLEX AREAS

We next discuss experimental results with more complex structures that have larger areas and multiple occluded objects. The robots use Wi-Fi RSSI measurements in this section, and the reconstructed images are obtained by using

the Rytov approximation of (8) for the received signal. Furthermore, the reconstructions are thresholded as described for the Wi-Fi imaging results of the “Experimental Imaging Results with Wi-Fi RSSI Signals” section. A comprehensive comparison of Rytov and LOS approximations for Wi-Fi-based imaging is given in [8].

Figure 6(a) shows the unknown area of interest, which has the size of 4.56 m × 5.74 m, while Figure 6(b) shows a horizontal cut of it. As shown, the occluded middle area has a larger dimension, making the imaging more challenging. Both the outer wall and the inner rectangle of this structure are made of concrete bricks. The unknown area to be imaged is marked with a red dashed line in two dimensions. Two robots take semiparallel routes along 0, 90, 80, and -10°. Figure 6(c) shows the reconstructed image with 2.2% measurements. The reconstruction quality is shown to be very good. For instance, the width of the inner block is imaged at 1.42 m with the original size being 1.39 m.

Next, Figure 7(a) shows the unknown area of interest, which has the size of 4.56 m × 5.74 m with two objects inside, while Figure 7(b) shows a horizontal cut of it. This whole area is made of concrete bricks. The unknown area to be imaged is

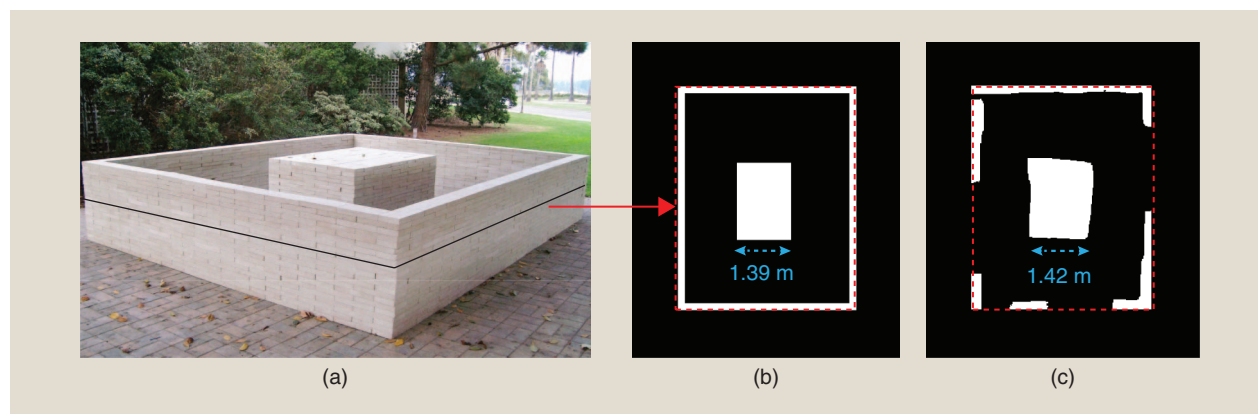


FIGURE 6. (a) The area of interest that is completely unknown, (b) a 2-D horizontal cut of it, which has the dimensions 4.56 m × 5.74 m, with the red dashed lines indicating the boundary of the unknown area to be imaged, and (c) reconstructed image with 2.2% Wi-Fi RSSI measurements using Rytov approximation.

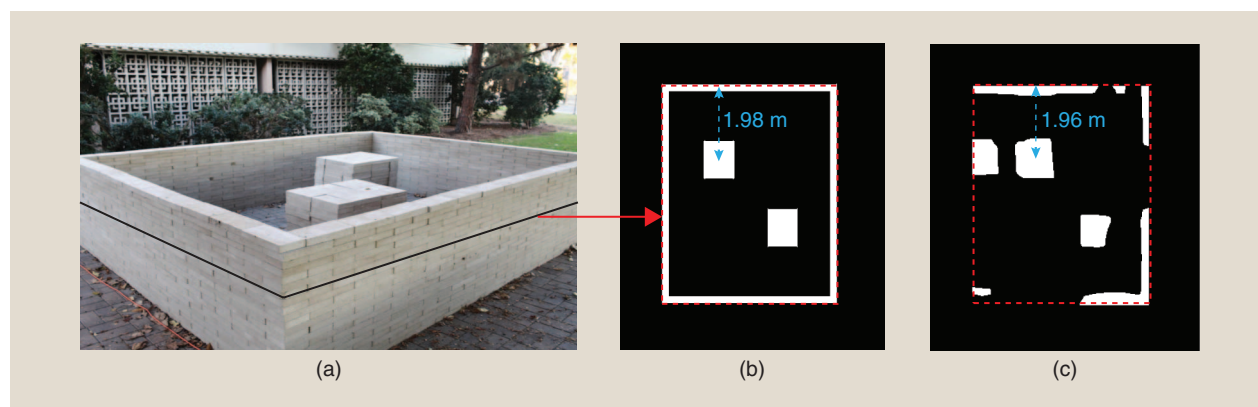


FIGURE 7. (a) The area of interest that is completely unknown, (b) a 2-D horizontal cut of it, which has the dimensions 4.56 m × 5.74 m, with the red dashed lines indicating the boundary of the unknown area to be imaged, and (c) reconstructed image with 2.6% Wi-Fi RSSI measurements using Rytov approximation.

marked with a red dashed line in two dimensions. A robotic imaging of this area with Wi-Fi is provided in [8]. Here, we summarize that result, but with an addition of Otsu's method, which improves the imaging quality considerably.

Two robots take semiparallel routes along 0, 90, 80, 10, and -10° . Figure 7(c) then shows the imaging result based on only 2.6% measurements. Because this area is more complex, we expect the imaging quality to drop as compared to the previous results. However, the details of the inner blocks and outer wall are still imaged well, as shown, and a sample dimension of 1.98 m is imaged at 1.96 m. As compared to the result of [8; Figure 10], several of the faint false images are not present anymore by using Otsu's method.

IMPACT OF ANTENNA DIRECTIONALITY

When showing the results with Wi-Fi RSSI measurements in the "Experimental Imaging Results with Wi-Fi RSSI Signals" section, the robots used the directional antenna of Figure 1(c). Using directional antennas when only having Wi-Fi RSSI measurements will help limit the scattering off of

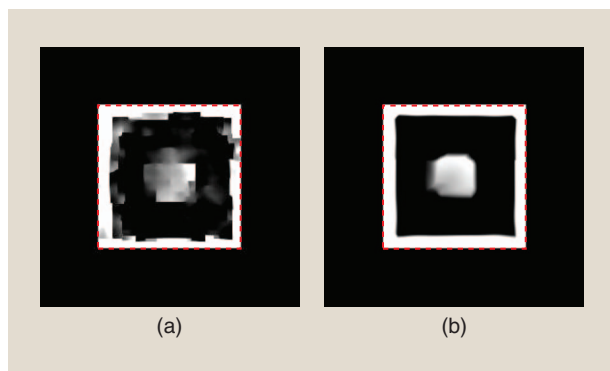


FIGURE 8. A comparison of imaging with omnidirectional and directional antennas for the case of Wi-Fi RSSI measurements and the unknown area of Figure 4(a). Rytov-based reconstructed image with 1.41% Wi-Fi RSSI measurements using (a) omnidirectional and (b) directional antennas. While we expect to lose some imaging quality with omnidirectional antennas, we can still see a fair amount of details because we can have a more optimized positioning of the Tx and Rx antennas with robots.

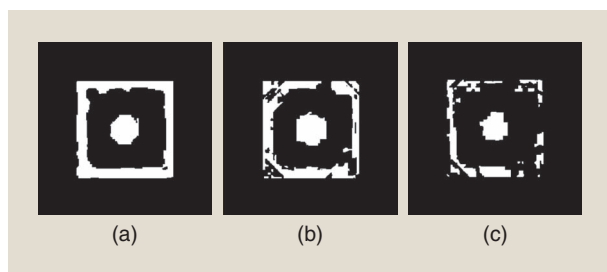


FIGURE 9. The effect of a large amount of localization error on robotic imaging. The reconstructed images with positioning error of standard deviation: (a) 0 cm, (b) 5 cm, and (c) 10 cm are shown. It is shown that even with a position error with a standard deviation of 10 cm per position, the area can still be imaged with reasonable quality.

the objects that are not directly on the LOS path between the Tx and Rx. In this section, we show the imaging result if the robots use an omnidirectional antenna instead, while imaging with Wi-Fi RSSI signals.

More specifically, the robots use a dipole antenna at 2.4 GHz, which comes with the robots, instead of the directional antenna of Figure 1(c). Figure 8 compares the imaging result of omnidirectional and directional cases for the unknown area of Figure 4(a), based on the same robotic routes and number of wireless transmissions of Figure 4. Rytov approximation is used in these results, and the area to be imaged is marked with a dashed red line. As expected, imaging with Wi-Fi RSSI signals and with omnidirectional antennas is more challenging. However, by using semiparallel robotic routes, the area can still be imaged, as shown. In other words, by using robots for imaging, we have created the possibility of optimizing the positioning of the antennas and subsequently extracting decent images from only Wi-Fi RSSI signals and omnidirectional antennas. In the next section, we extensively discuss the impact of robotic paths on imaging.

IMPACT OF ROBOT LOCALIZATION ERRORS

In imaging with unmanned vehicles, two robots move outside of the unknown area to collect wireless measurements, as discussed previously. Each robot estimates its own position and the position of the other robot when the wireless measurements are collected, based on the given constant speed. However, in harsh environments, there may be positioning errors, for instance, due to nonuniform robot speeds as a result of uneven ground conditions. Therefore, in this section, we evaluate the impact of a large amount of robot localization error on the reconstruction quality.

To analyze the effect of localization errors, we next manually add large errors to the measurement locations. We note that the locations in the experimental measurements are already subject to small errors. But for the purpose of the analysis of this section, we assume that the localization errors in our experiments were negligible and manually add errors to the location stamps. We then use these highly noisy measurement locations in the reconstructions. More specifically, we add a zero-mean Gaussian noise with a standard deviation of σ to both the x and y coordinates of the positions estimated by each robot. We use these noisy measurement locations in the reconstructions.

Figure 9 shows sample reconstructions with different amounts of localization noise ($\sigma = 5$ and $\sigma = 10$) for the case of Wi-Fi-based imaging of the unknown area of Figure 4(a), where the length and width of the wall are 2.98 m, thickness of the wall is 0.1 m, and the diameter of the occluded cylinder is 0.58 m. For comparison, we note that the errors encountered in our experiments are typically much smaller. For instance, in the experiments of the "Experimental Results" section, the ground vehicles experience a localization error with an average standard deviation of 3.6 cm along the route and 1.45 cm along the direction

perpendicular to the route. In this section, we then add an error with a standard deviation as high as 10 cm to each location in both x and y directions, which is much larger than the typical errors encountered in real experiments. While the imaging quality degraded for the case of $\sigma = 10$ as compared to $\sigma = 0$, we can still obtain an informative image despite the large amount of localization error. Furthermore, a good reconstruction can still be obtained up to a standard deviation of $\sigma = 25$ cm, which is much larger than the typical errors in actual experiments. Similar observations have been made for other areas, thus establishing the robust nature of the framework to robot localization errors.

ROBOTIC PATH PLANNING FOR IMAGING

In the previous sections, we extensively discussed two approaches, Wi-Fi-based and UWB-based, for robotic through-wall imaging and thoroughly validated them by experiments. We used two robots that moved in semiparallel routes, as described in the “A Foundation for Robotic Through-Wall Imaging” section, to image several real structures in our experiments. However, there are other possible routes that the robots can take, as established in [9]. Thus, for the sake of completion, in this section, we summarize the impact of the choice of the robotic routes on the imaging quality, building on [9] and highlighting the key insights.

We mainly focus on two broad motion patterns, termed *semiparallel* and *random*, which were introduced in the “Robotic Path Planning” section and Figure 3. As we shall see, properly designed semiparallel routes can be considerably informative for imaging. However, the robots may not be able to always traverse such routes due to environmental/time constraints. Then, random motion patterns can be used and can even have a better performance than the semiparallel ones under certain conditions, as we discuss in this section. We note that throughout this section, we use simulations for comparing different route designs. Specifically, for a given workspace and the routes for robots, we generate wireless measurements by using the LOS-based forward approximation. Still, the gained insights will be helpful when designing robotic routes in the experiments. We also note that the nature of this section is analytical in the sense that we explore the routes that could be most informative for imaging, with an emphasis on understanding the underlying tradeoffs.

DIVERSITY OF THE MEASUREMENTS

As defined in [9], let the spatial variations (jumps) of a two-dimensional (2-D) image along angle θ denote the variations of the line integral of the area, along lines orthogonal to the line at angle θ [e.g., see Figure 3(a)]. When the robots move on a semiparallel route at angle θ , the measurements then naturally have the potential of capturing the spatial variations (jumps) of the unknown space along the direction θ if the robots transmit/receive at a high-enough spatial resolution along that route. For instance, Figure 10 shows the 2-D cut of the occluded cylinder scenario and the corresponding real measurements

collected along a semiparallel route at 0° , by using directional antennas and sampling at 2-cm intervals with Wi-Fi signals. As shown, the measurements clearly reflect the spatial jumps of the unknown space along the 0° direction. Even without the use of directional antennas, we expect the variations in the power measurements along a semiparallel route to be correlated with the spatial changes of the material property along that route. Thus, a semiparallel route has the potential to capture the spatial changes of the area of interest along a particular route.

However, a semiparallel route at angle θ has a limited perspective of the unknown space, which is only along the direction θ , i.e., the robots can view the unknown space as a projection along only one direction. On the other hand, when the robots move in a random pattern, i.e., when they collect measurements from a few Tx/Rx position pairs in the workspace, they can potentially get multiple perspectives of the unknown space. However, in this case, the spatial jumps (variations) of the unknown space may not be clearly identified. In summary, the number of semiparallel routes, their

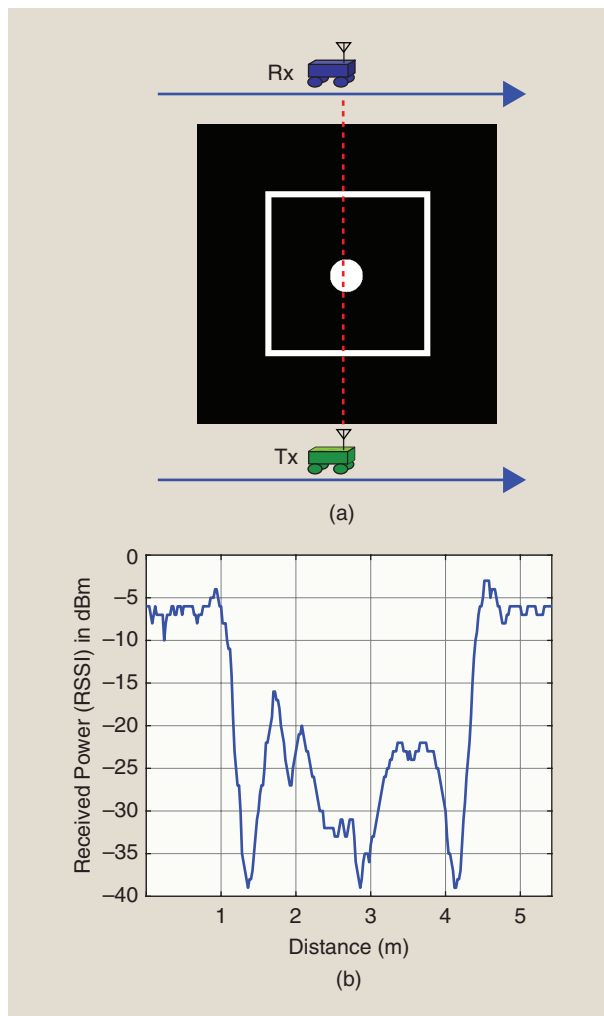


FIGURE 10. (a) The occluded cylinder scenario of Figure 4(a) with robots making measurements along the 0° route, and (b) the corresponding real Wi-Fi RSSI measurements.

choice, and the sampling resolution along each route can considerably affect the overall imaging performance.

Thus, we can ask the following question—given a fixed number of wireless measurements that the robots can make, over what kind of routes should they be distributed? We motivate the discussion by an example. Consider the occluded cylinder shown in Figure 4(a). Given an extremely small percentage of measurements of 0.77%, Figure 11(a) shows the reconstructed image when the robots collect the measurements at random Tx/Rx position pairs in the workspace. On the other hand, Figure 11(b) shows the corresponding reconstruction, when all the measurements are collected along the 0° robotic route. The semiparallel case is shown to perform worse in this example. More specifically, Figure 11(b) shows that the semiparallel route along 0° clearly identifies the jumps in the unknown space, but only along the 0° direction. On the other hand, although the case of a random route does not clearly identify the boundaries, it results in a better overall reconstruction in this case.

Next, we increase the number of measurements to 4.6% in Figure 11(b) and (c). In this case, the measurements of semiparallel routes are distributed along four routes of 0° , 90° , 45° , and 135° , while the measurements of the random pattern are collected at randomly distributed Tx/Rx position pairs outside of the unknown area. The reconstructions show that the semiparallel routes outperform in this case. This is because four semiparallel routes can now measure

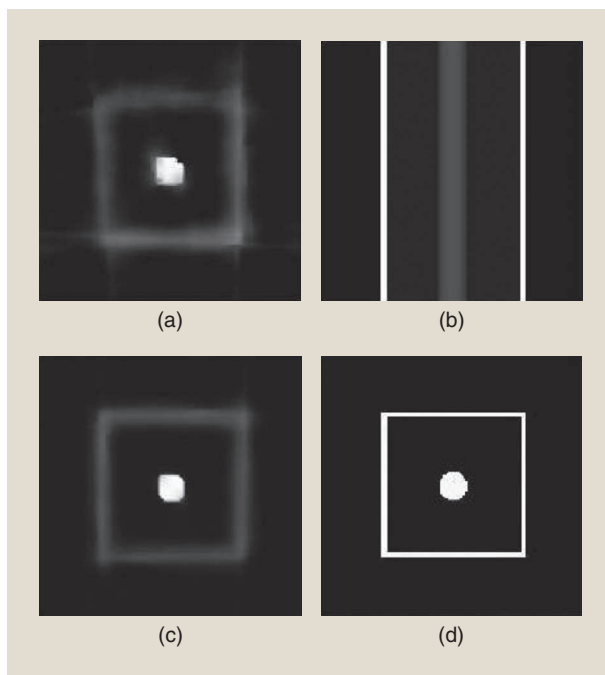


FIGURE 11. A comparison of semiparallel and random routes in imaging the occluded cylinder of Figure 4(a). (a) and (b) The imaging obtained with 0.77% measurements for (a) the case of random routes and (b) the case of semiparallel routes along one angle. (b) and (c) The imaging obtained with 4.6% measurements for (c) the case of random routes and (d) the case of semiparallel routes along four routes.

the jumps along a few informative angles, providing both spatial resolution along each route and an overall diversity of views.

In summary, we see that semiparallel routes can be considerably informative by capturing the spatial changes. However, it is important that they are diverse enough in terms of capturing the area from different perspectives. Therefore, given a number of wireless measurements, we need to identify the optimum number of angles over which they should be distributed. Distributing the measurements over a large number of angles results in more diversity at the cost of less spatial resolution along each route, presenting interesting tradeoffs. Furthermore, we need to identify which semiparallel routes (what angles) are the most informative. In the next section, we start by discussing the choice of optimal angles for semiparallel routes, followed by the optimum number of semiparallel routes.

OPTIMAL CHOICE OF ANGLES FOR SEMIPARALLEL ROUTES

As discussed in the previous section, a semiparallel route along a given direction θ can capture the spatial variations of the unknown space along angle θ . Hence, when considering the choice of the angles, moving along the directions that contain the most spatial variations (jumps) in the unknown space would be more optimal.

As an example, consider the occluded cylinder shown in Figure 4(a), the 2-D cut of which is shown in Figure 12(a)

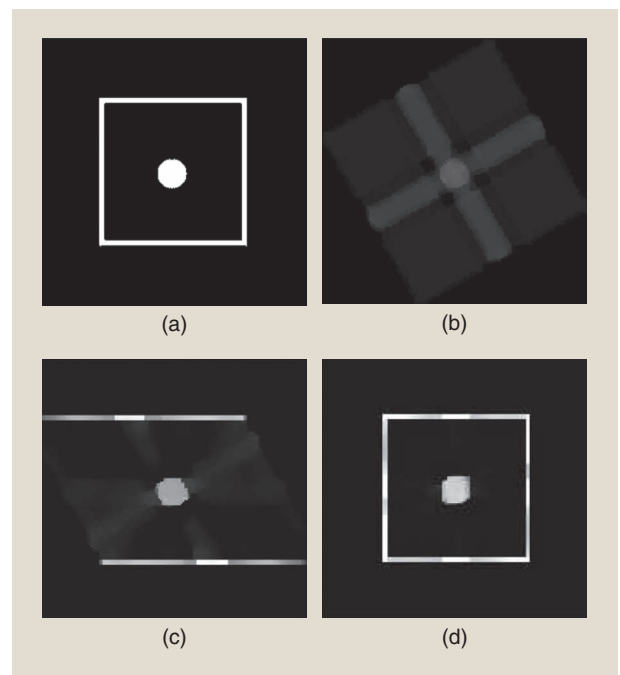


FIGURE 12. A comparison of imaging with different semiparallel route angles for the occluded cylinder. (a) The true image, (b) imaging with no routes along the jump angles, (c) imaging with one route along one jump angle, and (d) imaging with two routes along two jump angles. Making measurements along jump angles is shown to give a better reconstruction.

as well. This structure contains jumps mainly along 0° and 90° . Figure 12(b) shows the reconstruction when measurements are collected along 30° , 60° , 120° , and 150° and not along the main jump angles. It is shown that the information about the walls is completely missing in the reconstruction. Next, we make measurements along the 90° angle instead of 120° , while retaining the other angles. Figure 12(c) shows the reconstruction for this case. It is shown that jumps along the 90° direction are now identified. Finally, we replace two of the angles with 0° and 90° , which are the main jump directions for this structure. As shown in Figure 12(d), the reconstruction is almost exact. This toy example confirms that moving along the angles with the most spatial jumps can be considerably

informative for imaging. For a more formal information-theoretic proof of this for a simple structure, we refer the readers to our previous work [9]. We note that during their operation, the robots do not know the jump angles, as the area is completely unknown to them. Thus, the insight from the aforementioned analysis can be used in two manners. First, it could be used in sequential imaging, where the robots adapt their routes online based on the current reconstructed image. Second, several spaces have underlying patterns, for instance, in terms of orthogonality of walls, which can be used to design the initial routes by the robots.

OPTIMAL NUMBER OF ANGLES FOR SEMIPARALLEL ROUTES

Consider the case where the robots can make a given number of measurements. We next consider the choice of the number of angles along which the robots should distribute their measurements. Intuitively, if they collect these measurements over a large number of angles, they have more diversity in sampling the space from different perspectives while the sampling resolution along each angle will be less, as discussed earlier. In this section, we discuss this while considering the optimum choice of angles.

Figure 13 shows the imaging performance in terms of the normalized mean square error (NMSE), as a function of the number of angles, for three different structures shown on the left. For each structure, there is a given number of allowed measurements, as indicated in the legend. For each number of angles, first the angles corresponding to the directions of jumps are chosen. Then the remaining angles are chosen to have a uniform angle distribution. Furthermore, the total allowed measurements are distributed evenly among the given angles. For each structure, there is an optimum number of angles at which the imaging error is minimum, and this optimum strikes a balance between spatial resolution and diversity

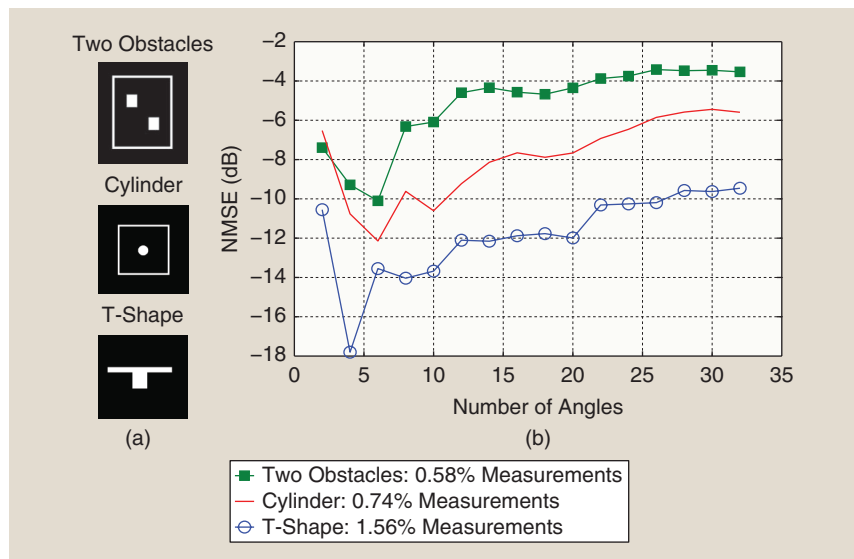


FIGURE 13. (a) The considered scenarios for the illustration of optimum number of angles and (b) the NMSE of imaging quality for the considered scenarios as a function of number of angles.

for the structure. For instance, this optimum is four for the T-shape, while it is six for the other cases. In general, we can see that, as the structure gets more complex, more randomization (diversity of views) may be needed through distributing the measurements among a larger number of angles [9].

CONCLUSIONS

The goal of this article was to provide a comprehensive foundation for the possibilities at the intersection of robotics and inverse scattering for through-wall imaging. More specifically, we considered high-resolution through-wall imaging of completely unknown spaces using unmanned vehicles. In our first case, we focused on through-wall imaging based on Wi-Fi RSSI signals, while in our second case, we considered imaging based on first-path power and ToA of UWB signals. The article presented a framework for robotic through-wall imaging based on proper path planning, sparse signal processing, and linearized wave modeling and confirmed it with several experimental results that involved imaging completely unknown spaces with a variety of materials. The UWB and Wi-Fi-based approaches were extensively compared. Furthermore, the impact of antenna directionality was demonstrated. Overall, the article can serve as a comprehensive reference for the possibilities created by using unmanned vehicles for through-wall imaging.

ACKNOWLEDGMENT

This work is funded by National Science Foundation Communications, Circuits, and Sensing Systems award number 1611254.

AUTHOR INFORMATION

Saandeep Depatla (saandeep@ece.ucsb.edu) received his M.S. degree in electrical and computer engineering from the University

of California Santa Barbara (UCSB) in 2014. Since 2013, he has been working toward his Ph.D. degree at UCSB, focusing on radio-frequency sensing.

Chitra R. Karanam (ckaranam@ece.ucsb.edu) received her M.S. degree in electrical and computer engineering from the University of California Santa Barbara (UCSB) in 2016, where she is currently pursuing her Ph.D. degree. Her research interests include radio-frequency sensing, robotics, and array signal processing.

Yasamin Mostofi (ymostofi@ece.ucsb.edu) is a professor at the University of California Santa Barbara and a recipient of the IEEE Control Systems Society Antonio Ruberti Prize, Presidential Early Career Award for Scientists and Engineers, National Science Foundation Faculty Early Career Development Program, and the IEEE Region 6 Outstanding Engineer Award.

REFERENCES

- [1] A. J. Devaney. (2000). Super-resolution processing of multi-static data using time reversal and MUSIC. [Online]. Available: https://www.researchgate.net/publication/242043772_Super-resolution_Processing_of_Multi-static_Data_Using_Time_Reversal_and_MUSIC
- [2] F. Soldovieri and R. Solimene, "Through-wall imaging via a linear inverse scattering algorithm," *IEEE Geosci. Remote Sens. Lett.*, vol. 4, no. 4, pp. 513–517, 2007.
- [3] H. Wang, R. M. Narayanan, and O. Z. Zhou, "Through-wall imaging of moving targets using UWB random noise radar," *IEEE Antennas Wireless Propag. Lett.*, vol. 8, pp. 802–805, 2009.
- [4] F. Ahmad and M. G. Amin. "Through-the-wall radar imaging experiments," in *Proc. 2007 IEEE Workshop Signal Processing Applications Public Security and Forensics*, pp. 1–5.
- [5] S. Depatla, A. Muralidharan, and Y. Mostofi, "Occupancy estimation using only Wi-Fi power measurements," *IEEE J. Sel. Areas Commun.*, vol. 33, no. 7, pp. 1381–1393, 2015.
- [6] A. Ghaffarkhah, A. Gonzales-Ruiz, and Y. Mostofi, "An integrated framework for obstacle mapping with see-through capabilities using laser and wireless channel measurements," *IEEE Sensors J.*, vol. 14, no. 1, pp. 25–38, Jan. 2014.
- [7] Y. Mostofi, "Cooperative wireless-based obstacle/object mapping and see-through capabilities in robotic networks," *IEEE Trans. Mobile Comput.*, vol. 12, no. 5, pp. 817–829, Jan. 2012. doi: 10.1109/TMC.2012.32.
- [8] S. Depatla, L. Buckland, and Y. Mostofi, "X-ray vision with only Wi-Fi power measurements using Rytov wave models," *IEEE Trans. Veh. Technol.*, vol. 64, no. 4, pp. 1376–1387, 2015.
- [9] A. Gonzalez-Ruiz and Y. Mostofi, "Cooperative robotic structure mapping using wireless measurements—a comparison of random and coordinated sampling patterns," *IEEE Sensors J.*, vol. 13, no. 7, pp. 2571–2580, 2013.
- [10] C. R. Karanam and Y. Mostofi, "3-D through-wall imaging with unmanned aerial vehicles using Wi-Fi," in *Proc. 16th ACM/IEEE Int. Conf. Information Processing in Sensor Networks*, 2017, pp. 131–142.
- [11] DecaWave. (2017). ScenSor EVK1000 Evaluation Kit. [Online]. Available: <http://www.decawave.com/>
- [12] D. Colton and A. Kirsch, "A simple method for solving inverse scattering problems in the resonance region," *Inverse Problems*, vol. 12, no. 4, p. 383, 1996.
- [13] Y. Wang and W. C. Chew, "An iterative solution of the two-dimensional electromagnetic inverse scattering problem," *Int. J. Imaging Syst. Technol.*, vol. 1, no. 1, pp. 100–108, 1989.
- [14] W. C. Chew and Y. Wang, "Reconstruction of two-dimensional permittivity distribution using the distorted Born iterative method," *IEEE Trans. Med. Imag.*, vol. 9, no. 2, pp. 218–225, 1990.
- [15] P. Van Den Berg, A. Van Broekhoven, and A. Abubakar, "Extended contrast source inversion," *Inverse Problems*, vol. 15, no. 5, p. 1325, 1999.
- [16] M. Pastorino, "Stochastic optimization methods applied to microwave imaging: A review," *IEEE Trans. Antennas Propag.*, vol. 55, no. 3, pp. 538–548, 2007.
- [17] A. J. Devaney, "Inversion formula for inverse scattering within the Born approximation," *Opt. Lett.*, vol. 7, no. 3, pp. 111–112, 1982.
- [18] G. Oliveri, L. Poli, P. Rocca, and A. Massa, "Bayesian compressive optical imaging within the Rytov approximation," *Opt. Lett.*, vol. 37, no. 10, pp. 1760–1762, 2012.
- [19] A. Massa, P. Rocca, and G. Oliveri, "Compressive sensing in electromagnetics—a review," *IEEE Antennas Propag. Mag.*, vol. 57, no. 1, pp. 224–238, 2015.
- [20] L. Poli, G. Oliveri, and A. Massa, "Microwave imaging within the first-order Born approximation by means of the contrast-field Bayesian compressive sensing," *IEEE Trans. Antennas Propag.*, vol. 60, no. 6, pp. 2865–2879, 2012.
- [21] Q. Huang, L. Qu, B. Wu, and G. Fang, "UWB through-wall imaging based on compressive sensing," *IEEE Trans. Geosci. Remote Sens.*, vol. 48, no. 3, pp. 1408–1415, 2010.
- [22] M. J. Burfeindt, J. D. Shea, B. D. Van Veen, and S. C. Hagness, "Beamforming-enhanced inverse scattering for microwave breast imaging," *IEEE Trans. Antennas Propag.*, vol. 62, no. 10, 2014.
- [23] P. Kosmas and C. M. Rappaport, "Time reversal with the FDTD method for microwave breast cancer detection," *IEEE Trans. Microw. Theory Techn.*, vol. 53, no. 7, pp. 2317–2323, 2005.
- [24] J. Marcum, "A statistical theory of target detection by pulsed radar," *IRE Trans. Inform. Theory*, vol. 6, no. 2, pp. 59–267, 1960.
- [25] Y. Huang, P. V. Brennan, D. W. Patrick, I. Weller, P. Roberts, and K. Hughes, "FMCW based MIMO imaging radar for maritime navigation," *Prog. Electromagnetics Res.*, vol. 115, pp. 327–342, 2011.
- [26] J. C. Curlander and R. N. McDonough, *Synthetic Aperture Radar*. New York: Wiley, 1991.
- [27] F. Sabath, D. V. Giri, F. Rachidi, and A. Kaelin, *Ultra-Wideband, Short-Pulse Electromagnetics 7*. New York: Springer-Verlag, 2007.
- [28] R. Chandra, A. Gaikwad, D. Singh, and M. J. Nigam, "An approach to remove the clutter and detect the target for ultra-wideband through-wall imaging," *J. Geophys. Eng.*, vol. 5, no. 4, p. 412, 2008.
- [29] F. Ahmad, M. G. Amin, and S. A. Kassam, "Synthetic aperture beamformer for imaging through a dielectric wall," *IEEE Trans. Aerosp. Electron. Syst.*, vol. 41, no. 1, pp. 271–283, 2005.
- [30] F. Ahmad, J. Qian, and M. G. Amin, "Wall clutter mitigation using discrete prolate spheroidal sequences for sparse reconstruction of indoor stationary scenes," *IEEE Trans. Geosci. Remote Sens.*, vol. 53, no. 3, pp. 1549–1557, 2015.
- [31] Y. S. Yoon and M. G. Amin, "Spatial filtering for wall-clutter mitigation in through-the-wall radar imaging," *IEEE Trans. Geosci. Remote Sens.*, vol. 47, no. 9, pp. 3192–3208, 2009.
- [32] F. H. C. Tivive, A. Bouzerdoum, and M. G. Amin, "A subspace projection approach for wall clutter mitigation in through-the-wall radar imaging," *IEEE Trans. Geosci. Remote Sens.*, vol. 53, no. 4, pp. 2108–2122, 2015.
- [33] Y. Mostofi and A. Gonzalez-Ruiz, "Compressive Cooperative Obstacle Mapping in Mobile Networks," in *Proc. Military Commun. Conf.*, pp. 947–953, San Jose, CA, Oct. 2010.
- [34] W. C. Chew, *Waves and Fields in Inhomogeneous Media*, vol. 522. Piscataway, NJ: IEEE Press, 1995.
- [35] DecaWave_group. (n.d.). [Online]. Available: https://groups.google.com/forum/#!forum/decawave_group
- [36] M. G. Amin, *Through-the-Wall Radar Imaging*. Boca Raton, FL: CRC, 2016.
- [37] E. Candès, J. Romberg, and T. Tao, "Robust uncertainty principles: Exact signal reconstruction from highly incomplete frequency information," *IEEE Trans. Inf. Theory*, vol. 52, no. 2, pp. 489–509, 2006.
- [38] D. L. Donoho, "Compressed sensing," *IEEE Trans. Inf. Theory*, vol. 52, no. 4, pp. 1289–1306, 2006.
- [39] D. Needell and R. Vershynin, "Uniform uncertainty principle and signal recovery via regularized orthogonal matching pursuit," *Found. Computational Mathematics*, vol. 9, no. 3, pp. 317–334, 2009.
- [40] C. Li, W. Yin, and Y. Zhang, "Users guide for TVAL3: TV minimization by augmented Lagrangian and alternating direction algorithms," *CAAM Rep.*, vol. 20, pp. 46–47, 2009.
- [41] N. Otsu, "A threshold selection method from gray-level histograms," *Automatica*, vol. 11, pp. 285–296, 1975.
- [42] MobileRobots Inc. (2016). [Online]. Available: <http://www.mobilerobots.com>
- [43] Laird Technologies. (2017). [Online]. Available: <http://www.lairdtech.com/Products/Antennas-and-Reception-Solutions/>
- [44] *IEEE Standard for Local and Metropolitan Area Networks—Part 15.4: Low-Rate Wireless Personal Area Networks (LR-WPANs)*, IEEE Standard 802.15.4-2011, 2011.

